Factors Influencing Model Skill for Hindcasting Shallow Water Currents during Hurricane Andrew

TIMOTHY R. KEEN

Naval Research Laboratory, Oceanography Division, Stennis Space Center, Mississippi

SCOTT M. GLENN

Institute of Marine and Coastal Sciences, Rutgers University, New Brunswick, New Jersey

(Manuscript received 2 December 1996, in final form 8 May 1997)

ABSTRACT

Hurricane Andrew made landfall in the Gulf of Mexico after crossing directly over several moored current meter arrays deployed on the Louisiana–Texas shelf. The resulting three-dimensional current, temperature, and salinity time series are used in a quantitative analysis of the factors affecting the hindcast skill of ocean circulation models. This paper describes parameters for quantifying a model's skill at matching both maximum currents and time series at specific locations and depths. It then briefly discusses the following factors with respect to currents hindcast with the Princeton Ocean Model: 1) model domain size; 2) horizontal resolution, including the bathymetry and coastline; 3) vertical resolution (i.e., number of model levels); 4) the surface drag formulation; 5) the bottom drag coefficient; 6) turbulent mixing parameters and sources of turbulence; and 7) the initial temperature field. Model performance is found to be most dependent on parameters within the turbulent energy closure scheme and the initial temperature and salinity distributions. The best overall model performance is gained by adjusting one of the closure scheme coefficients (B_1) that decreases turbulence dissipation (and increases mixing where a density gradient exists). Results incorporating wave breaking and a depth-dependent initial temperature field, however, are also reasonable, and differences between the model skill parameters are insufficient to determine which approach is preferable.

1. Introduction

Time series observations from fixed moorings can be used to evaluate a model's skill at reproducing an event of a few days' duration, during which physical, chemical, and biological processes operate at timescales of hours. A few examples are phytoplankton blooms, tidal mixing fronts, river plumes, meteorological fronts, tropical and extratropical cyclones, and coastal eddies. When temporal and spatial scales are reduced sufficiently to permit such processes to be simulated, short-term fluctuations and spatial variability become the dominant indicators of model performance. The passage of a tropical storm is an excellent example of this kind of flow event. The coastal currents produced by these storms are especially suitable for model evaluation in shallow water because both baroclinic and barotropic storm flows are strong enough to be identified for short periods, even when shelf- and basin-scale flows are present.

To confidently use numerical models to study the dynamics of coastal flows during storms, it is important to first validate the numerical models with observations. This has proven problematical because of the difficulties in making measurements at just the right place and time. One example of a successful storm observation program is the passage of Tropical Storm Delia (1973) over the Buccaneer oil platform on the Texas continental shelf. Shallow water currents for this storm have been hindcast by Forristall et al. (1977), Spaulding and Isaji (1987), and Keen and Slingerland (1993). All three studies reasonably reproduced the Buccaneer currents, located directly along the storm track, but because of the lack of observations at more than one site, validation of model-predicted currents at other locations was not possible. Spatially distributed current measurements were made on the Louisiana continental shelf during Hurricane Andrew in 1992 (Cardone et al. 1994). The simultaneous validation of numerical model results at several moorings gives the user greater confidence in the model-predicted currents away from the individual measurement sites.

This paper undertakes such a comparison by first describing two quantitative skill indices for model performance, and then calculating these parameters for a series of model hindcasts using time series of currents measured on the Louisiana shelf during Hurricane Andrew. The results will be used to address the following questions that

Corresponding author address: Dr. Timothy R. Keen, Naval Research Laboratory, Code 7322, Stennis Space Center, MS 39529.
E-mail: keen@nrlssc.navy.mil

arise in attempting to assess the accuracy and improve the quality of shallow water current hindcasts.

1) Using available measurements for a flow event with a strong signal, how accurate are the model currents in a spatial and temporal sense?
2) Can the performance of the model, as described by a quantitative skill index, be substantially improved by modifying the numerics or physics without resorting to significant ad hoc ''tuning?''
3) Can a quantitative comparison between measured and model currents be used to identify specific areas in the model formulation that require improvement?

2. Approach

The approach in this study is to use time series of model and measured currents at a number of locations to calculate indices for model skill at matching current peaks and reproducing time series. These indices are then used to describe the model's response to varying model parameters. Although there are a large number of parameters that can be adjusted to improve a model's performance, we will focus on three that could be termed numerical: 1) model domain size; 2) horizontal resolution, including the bathymetry and coastline; and 3) vertical resolution (i.e., number of model levels); and four that describe the physical environment: 1) the surface drag formulation; 2) the bottom drag coefficient; 3) turbulent mixing parameters and sources of turbulence; and 4) the initial temperature field.

Hindcast currents are calculated by the finite-difference Princeton Ocean Model (POM; Mellor 1993). POM is a primitive equation model with conservation equations for momentum, temperature, salinity, and turbulence variables. The finite-difference equations are solved on an Arakawa C grid using a split-mode solution scheme for the external and internal modes. Vertical mixing is calculated by the Mellor–Yamada level 2.5 closure (henceforth MY2.5) model (Mellor and Yamada 1982).

A number of numerical experiments have been run. Four model grids are used (Fig. 1; Table 1): 1) the northern Gulf of Mexico (NGoM) with a cell size of 0.1° and 10 σ levels, 2) the NGoM using the same horizontal resolution and 20 σ levels, 3) the NGoM with a cell size of 0.05° and 20 σ levels, and 4) the entire Gulf of Mexico (GoM) with a cell size of 0.1° and 20 σ levels. Model bathymetry for the NGoM grids was derived from the raw soundings obtained from the National Ocean Service (NOS). These data were gridded to 15 s. This gridded bathymetry was then interpolated to the model grids. The GoM bathymetry is from the NOS 0.01° database. All grids are restricted to a minimum depth of 8 m, and all wet grid points with shallower water depths were assigned this value.

3. Hurricane Andrew

After crossing the Florida Peninsula, Hurricane Andrew (Fig. 2) entered the Gulf of Mexico at 1200 GMT 24 August with a central pressure of approximately 950 mbar. Wind and wave fields (Cardone et al. 1994) have been hindcast for the period, Year Day (YD) 236.417 to YD 239.0 (GMT), at frequencies of 30 min for winds and 1 h for waves. The horizontal resolution of these fields is 0.1°. Wind speed and direction at 20 m, significant wave height, peak wave frequency, and wave travel direction are available as input to the circulation model. The accuracy of these fields is discussed by Cardone et al. (1994). The grid used for the wind and wave hindcasts extends from the west Florida coast to 94.5°W and from 24°N to the northern coast of the Gulf of Mexico. The wind and wave fields were interpolated to the circulation grids in Fig. 1.

At YD 236.898 (Fig. 3a), the hurricane eye was more than 500 km east of the Louisiana–Texas (LATEX) observation program moorings seen in Fig. 2, and hindcast winds were characterized by a broad easterly flow within the central Gulf of Mexico. Twelve hours later (Fig. 3b), the storm was approaching Louisiana and wind stresses exceeded 0.1 N m^{-2} within 100 km of the eye. Wind stresses remained low over the moorings, however. The eye was over the eastern moorings at YD 237.894 (Fig. 3c) and maximum stresses exceeded 2 N m^{-2} near the storm center. The wind direction was now changing rapidly at the moorings because of the advance of the eye across the study area. By YD 238.393 (Fig. 3d), the wind direction had reversed over the eastern mooring array, while stresses remained at about 1 N m^{-2}. The wind field across the mooring array was strongly convergent at this time as well.

At YD 236.898 (Fig. 4a), waves were low over the north central Gulf of Mexico, and it was not until 12 h later (Fig. 4b) that storm waves occurred near the Mississippi River delta. By YD 237.894 (Fig. 4c), waves exceeded 11 m over the eastern mooring array with a rapid decrease in significant wave heights over the shelf. The combination of decaying storm waves and fetch-limited wave growth for offshore winds produced a moderate wave field at YD 238.393 (Fig. 4d).

Hurricane Andrew passed directly over two cross-shelf lines of LATEX moored current meters (Fig. 2), and continuous time series were collected at 13 current meters (Table 2). This dataset (Fig. 5) clearly reveals the direct effect of the storm as well as near-inertial oscillations generated by the storm's passage. Comparison of surface and deep currents at the slope moorings (Figs. 5a and 5b) indicate that the storm-wind momentum flux did not penetrate to a depth of 100 m. Temperature and salinity profiles measured immediately prior to Andrew (Fig. 6) indicate a thermocline at a depth of less than 50 m beneath the surface. The temperature after the storm at depths of 11 and 100 m at mooring 13 was 24.5° and 16°C, respectively (Cardone et al. 1994), suggesting that the thermocline was not destroyed by the hurricane.

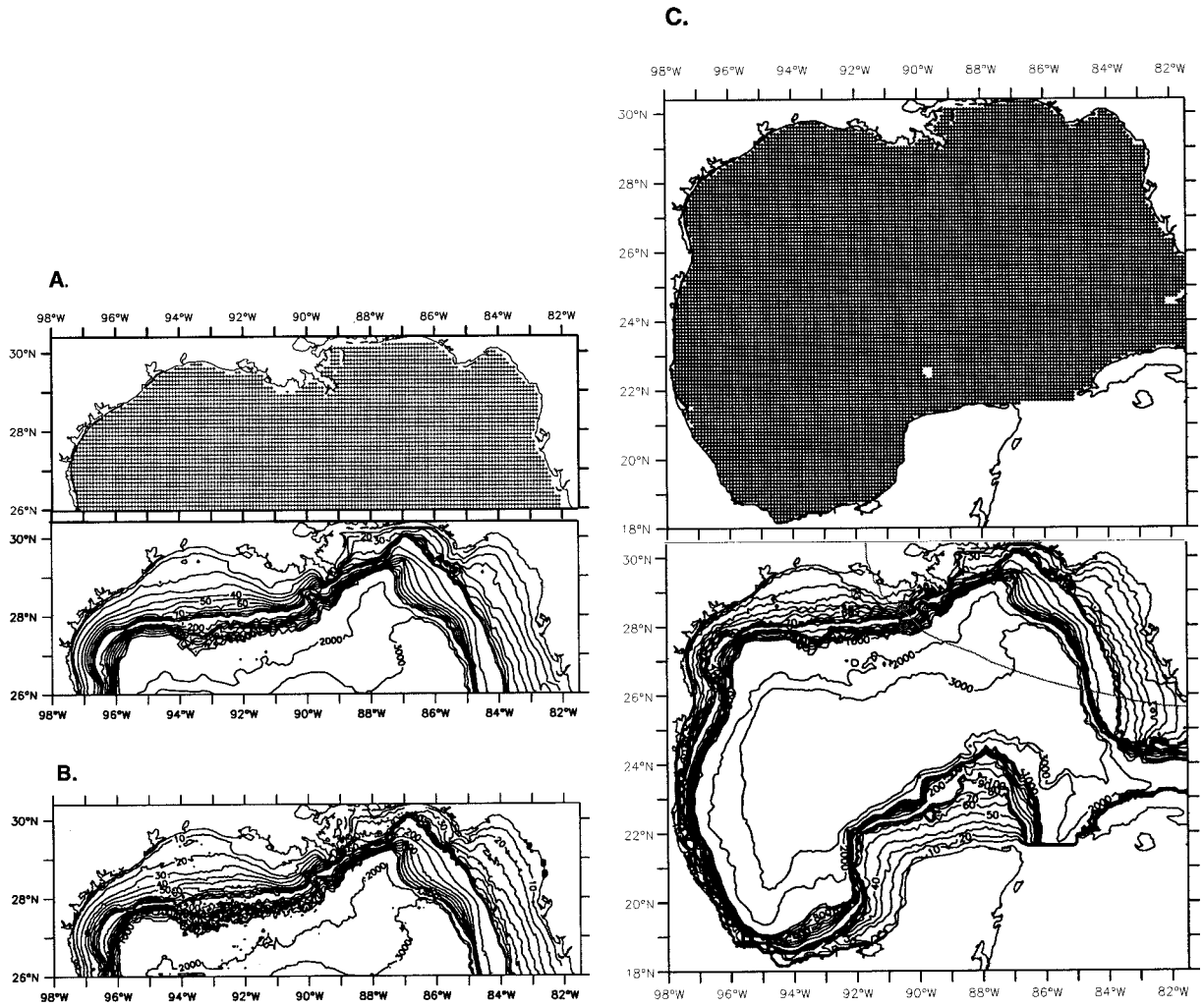

FIG. 1. Model grids. (a) Upper: Grid for Northern Gulf of Mexico (NGoM) domain with a cell size of 0.1°. Lower: Bathymetry regridded from 15′ gridded NOS raw data. (b) Bathymetry for NGoM domain with a cell size of 0.05°, regridded from 15′ gridded NOS raw data. (c) Upper: Grid for Gulf of Mexico domain with a cell size of 0.1°. Lower: Bathymetry regridded from the NOS 0.01° database. All grids were hand edited to match the 1:70 000 high-resolution coastline. Note that the coastline in the figures is the low-resolution CIA coastline.

4. Skill indices

a. Peak currents

Marine engineering design applications frequently require predictions of the peak current speeds, and their timing relative to storm waves and astronomical tides. The accuracy of a model for these purposes can be assessed by calculating the differences between the model and observed current speed and timing (Keen and Glenn 1996). To determine if this difference is meaningful, it should be normalized by an appropriate scale value. Given a set of N moorings, with an observed time series available for each, the normalized peak current speed and time differences are found from

$$\mathrm{SD}_i = 100 \times \frac{\mathrm{SP}_{mi} - \mathrm{SP}_{oi}}{\mathrm{SP}_{oi}}$$

and

$$\mathrm{TD}_i = 100 \times \frac{\mathrm{TP}_{mi} - \mathrm{TP}_{oi}}{\mathrm{TP}_S}, \qquad (1)$$

where i is the mooring number; SP_{mi} and SP_{oi} are the peak current speeds from the model and observations;

TABLE 1. Model grids used in this study.

Grid	Extent	σ levels	Cell size
1	26°–30.4°N (489 km) 82°–98°W (1570 km)	10	0.1° (11.1 km)
2	26°–30.4°N (489 km) 82°–98°W (1570 km)	20	0.1° (11.1 km)
3	26°–30.4°N (489 km) 82°–98°W (1570 km)	20	0.05° (5.56 km)
4	18°–30.4°N (1378 km) 81.5°–98°W (1613 km)	20	0.1° (11.1 km)

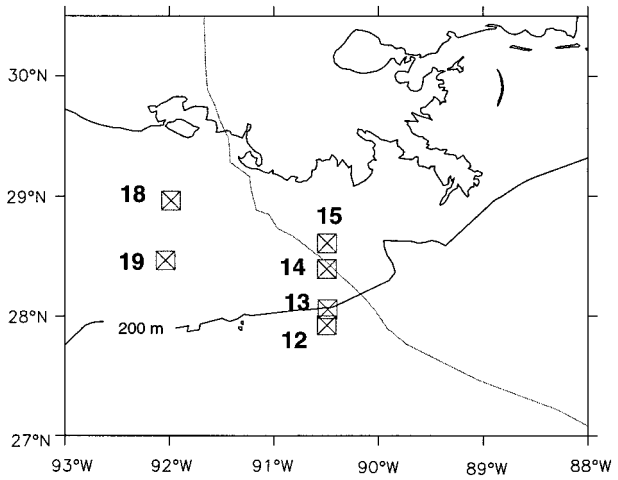

FIG. 2. Map showing location of LATEX moorings and track of Hurricane Andrew's eye.

and TP_{mi} and TP_{oi} are the times at which the peaks occur in the model and observations, respectively. If the speed difference $SD_i = 0$, the model perfectly matches the observed peak speed. Positive values imply the model is overpredicting the currents, and negative values indicate underprediction. Positive values of TD_i indicate that the model takes too long, and negative values indicate premature occurrence of the peak currents. The time differences are normalized by a scale interval for the event T_s, which must be defined. Because of the variability and complex current histories measured at some of the stations, no single value of T_s could be defined. Instead, the storm duration T_s was found by inspection of the highest peak that occurs within each measured time series (peak current time differences in hours can be found by multiplying the value of TD in Table 5 by the duration T_s).

The normalized peak speed and time differences are combined into four parameters representing the model fit to the spatially variable observed signal. First, average speed and time differences are found:

$$\mathrm{SD}_A = \frac{1}{N}\sum_{i=1}^{N} \mathrm{SD}_i$$

and

$$\mathrm{TD}_A = \frac{1}{N}\sum_{i=1}^{N} \mathrm{TD}_i. \tag{2}$$

Assuming that the SD_i and TD_i estimates are independent, the average permits detection of a bias in the model. An unbiased model will have an average of zero. The magnitude of the ensemble difference can be evaluated using rms normalized speed and time differences, given by

$$\mathrm{SD}_R = \sqrt{\frac{1}{N-1}\sum_{i=1}^{N} (\mathrm{SD}_i - \mathrm{SD}_A)^2}$$

and

$$\mathrm{TD}_R = \sqrt{\frac{1}{N-1}\sum_{i=1}^{N} (\mathrm{TD}_i - \mathrm{TD}_A)^2}. \tag{3}$$

These four parameters describe the overall model performance around the spatially and temporally variable storm current peaks. Since peak storm currents occur near the surface, these parameters are calculated for surface currents only at current meters ranging in depth from 3 to 12 m.

b. Time series performance

The goodness-of-fit between the time series of the model and observed currents can be described by the following reliability index (Leggett and Williams 1981):

$$\mathrm{RI}_i = \frac{1 + \sqrt{\frac{1}{T}\sum_{t=1}^{T}\left[\frac{1 - Y_{ti}/X_{ti}}{1 + Y_{ti}/X_{ti}}\right]^2}}{1 - \sqrt{\frac{1}{T}\sum_{t=1}^{T}\left[\frac{1 - Y_{ti}/X_{ti}}{1 + Y_{ti}/X_{ti}}\right]^2}}, \tag{4}$$

where i is the mooring number; T is the total number of pairs of data points in the time series; Y_{ti} is the observation at mooring i for time t; X_{ti} is model result at the same location and time. The model predictions are accurate within a factor of RI, that is, the observed values fall within 1/RI and RI times the corresponding predicted values. A value of 1 indicates a perfect time–space match, and as the model predictions and observations diverge, the reliability index grows. For example, if the model is a uniform 10% high or low, RI = 1.1 and 1.11, respectively. If the model is uniformly 50% high RI = 1.5, and if it is 50% low, RI = 2.27. This technique has been used to assess dynamic water quality model predictions (Martin 1988) and temporally and spatially variable suspended sediment profiles predicted by a bottom boundary layer model (Bedford and Lee 1994).

The RI can be calculated for a specific variable at each mooring, and the following average reliability index can be found:

$$\mathrm{RI}_A = \frac{1}{N}\sum_{i=1}^{N} \mathrm{RI}_i \tag{5}$$

This statistic allows both spatial and temporal comparisons to be unified in one parameter. Although it is practical to calculate a single parameter like RI_A when examining several factors affecting model skill, the individual RI_i values are useful for evaluating the spatial influence of specific factors.

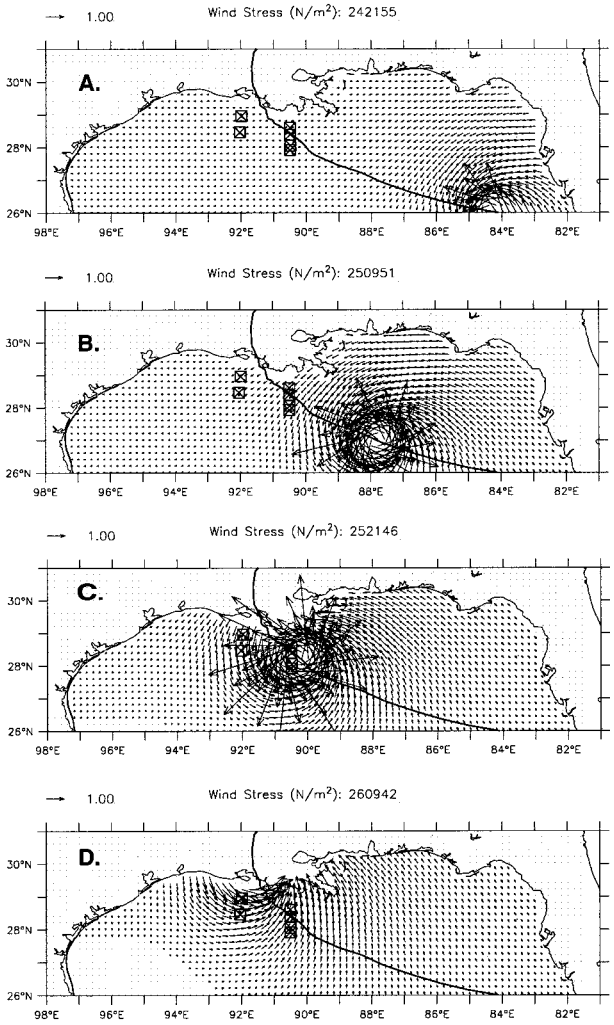

FIG. 3. Maps of hindcast wind stresses (N m^{-2}) at 12-h intervals for Hurricane Andrew simulation period. (a) 2155 GMT 24 August (YD 236.898), (b) 0951 GMT 25 August (YD 237.396), (c) 2146 GMT 25 August (YD 237.894), and (d) 0942 GMT 26 August (YD 238.393).

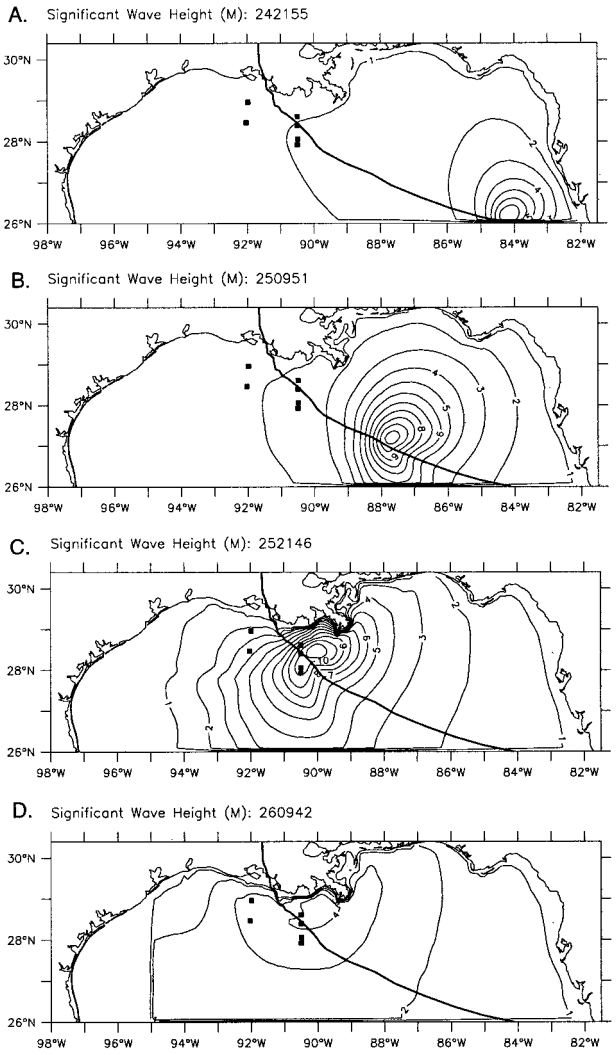

FIG. 4. Maps of hindcast significant wave height H_s (m) at 12-h intervals for Hurricane Andrew simulation period. (a) 2155 GMT 24 August (YD 236.898), (b) 0951 GMT 25 August (YD 237.396), (c) 2146 GMT 25 August (YD 237.894), and (d) 0942 GMT 26 August (YD 238.393). Contour interval is 1 m.

5. Hindcast results

A large number of numerical simulations were completed in an effort to improve the model predictions relative to the observations. For the purpose of this study, we will focus on several hindcasts (Table 3) that indicate the sensitivity of the model to numerical and environmental parameters, as well as the initial temperature field. Not every combination of changes is examined, but factors that would contribute most to improving the model's skill will be discussed in this section.

a. Model domain

Two model domains are used (Table 3): the GoM and the NGoM, from 26°N northward (Fig. 1). The larger domain is used in run 72 and the NGoM domain is used in run 59. Both domains have a horizontal grid resolution of 0.1° (~11.1 km) and use 20 σ levels. Peak surface current speed differences (Table 4) are slightly smaller for run 72 at moorings 12, 14, and 18, and larger at moorings 13 and 19. Peak surface currents in the

TABLE 2. Location of LATEX current meters for this study.

Mooring	Longitude	Latitude	Meter depth			Water depth
12	90.494598	27.923870	12	100		505
13	90.485878	28.057529	12	100	190	200
14	90.492867	28.394569	11	37		47
15	90.491577	28.608299	10	17		20
18	91.982719	28.962730	10	19		22
19	92.034798	28.465170	3	47		51

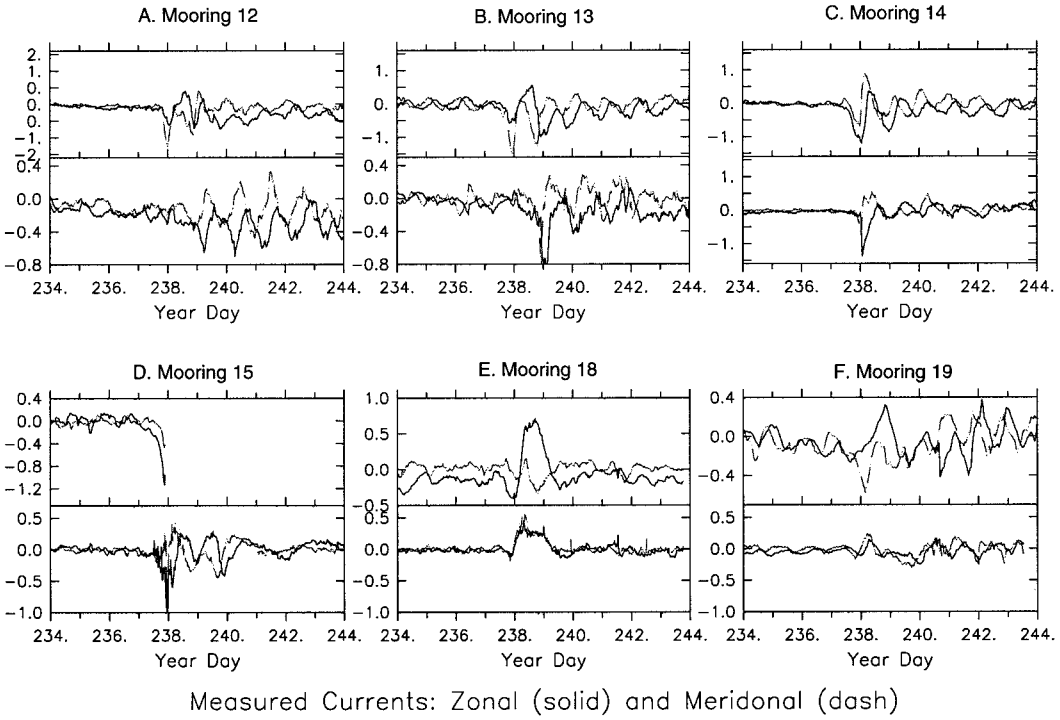

FIG. 5. Time series of measured currents (m s^{-1}) at LATEX moorings. (a) Mooring 12 (depth = 505 m): Upper: 12 m, lower: 100 m. (b) Mooring 13 (depth = 200 m): Upper: 12 m, lower: 100 m. (c) Mooring 14 (depth = 47 m): Upper: 11 m, lower: 37 m. (d) Mooring 15 (depth = 20 m): Upper: 10 m, lower: 17 m. (e) Mooring 18 (depth = 22 m): Upper: 10 m, lower: 19 m. (f) Mooring 19 (depth = 51 m): Upper: 3 m, lower: 47 m. Solid line is east–west component and dashed line is north–south.

large domain occur slightly earlier (Table 5) east of the storm track and later to the west. The reliability indices (Table 6) for the upper current meters are very close in runs 72 and 59, but the skill of run 72 improves at the deeper current meters, except at moorings 12 and 15. Overall, reductions in RI at moorings 18 and 19 contribute to a value of 2.32 for RI_A for run 72, compared to 2.62 for run 59. The hindcast skill of these two runs is very similar for the surface current meters, however.

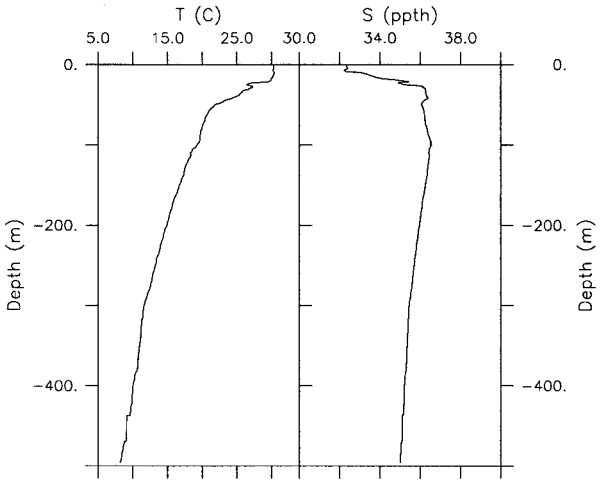

FIG. 6. Temperature and salinity profiles measured at mooring 13 on 24 August, and used as initial condition for all hindcasts except runs 85, 88, and 89.

b. Horizontal grid resolution

Higher horizontal grid resolution is necessary for computing coastal flows, but limitations on computer resources preclude using extremely large grids for most

TABLE 3. Conditions for numerical experiments.

Run	Initial T/S	Grid size	σ levels	C_d	k_{bc}	Closure
55	1D	0.1	10	0.002	0.01	Std
56	1D	0.1	20	0.002	0.01	Std
57	1D	0.1	20	0.002	0.1	Std
58	1D	0.1	20	0.002	0.001	Std
59	1D	0.1	20	0.002	0.1	$B_1 = 40$
61	1D	0.1	20	Wind	0.1	$B_1 = 40$
62*	1D	0.1	20	Wave	0.1	$B_1 = 40$
72**	1D	0.1	20	0.002	0.1	$B_1 = 40$
81	1D	0.05	20	0.002	0.1	$B_1 = 40$
85	3D	0.05	20	0.002	0.1	$B_1 = 40$
87	1D	0.05	20	0.002	0.1	Std/wave
88	3D	0.05	20	0.002	0.1	Std/wave
89*	3D	0.05	20	0.002	0.1	Std

* Incomplete hindcast.
** Entire Gulf of Mexico domain (see Table 1).

TABLE 4. Normalized peak surface current speed differences, SD (%).

Mooring	Experiment													
	SP_o*	55	56	57	58	59	61	62**	72	81	85	87	88	89**
12	138.0	40.7	55.3	55.5	55.4	1.84	70.9	78.5	1.45	−2.43	−12.8	1.98	−18.5	32.2
13	155.0	48.1	44.0	44.3	44.1	0.19	69.9	82.9	−4.57	4.96	−2.31	7.02	−7.07	50.0
14	130.0	125.0	128.0	129.0	128.0	90.2	183.0	201.0	79.9	92.9	88.7	66.1	92.1	116.0
18	77.1	12.1	30.9	27.7	37.8	5.47	82.8	199.0	3.39	7.16	10.8	5.11	18.8	108.0
19	58.7	91.3	107.0	101.0	111.0	34.0	75.3	45.5	51.6	22.6	24.0	−12.5	3.02	111.0
SD_A	112.0	63.5	73.1	71.5	75.3	26.3	96.5	121.0	26.3	25.0	21.7	13.6	17.7	83.6
SD_R	—	44.7	42.2	42.2	41.3	38.2	48.9	73.3	37.4	39.0	40.0	30.4	43.8	39.4

* Surface current speed (cm s^{-1}).
** Incomplete hindcast.

applications. Thus, a compromise must often be reached between the opposing objectives of resolving complex coastal geometry and running the model in a reasonable period of time. For example, the GoM domain discussed above is inconveniently large to use a cell size of 0.05°, so it becomes necessary to evaluate the effect of horizontal resolution using the NGoM domain. The two grid sizes compared here are 0.1° (~11.1 km) and 0.05° (~5.55 km); run 81 uses the smaller cell and run 59 uses the larger cell size. The values of SD for the higher-resolution grid (Table 4) are slightly greater everywhere except at mooring 19, where they are approximately 34% smaller than in run 59. Phase differences (Table 5) are substantially the same for these two runs except for a large reduction for the higher-resolution grid at mooring 18. Improvements in run 81 are also nonuniform for RI (Table 6). Model skill decreases slightly at moorings 12, 13, and 14 only. The greatest increase in skill associated with the higher-resolution grid occurs at the bottom current meters at moorings 13, 18, and 19, and it is sufficient to decrease RI_A from 2.62 (run 59) to 2.31. This distribution of error suggests that where a complex interplay of wind, coastal setup, and stratification exists, higher-resolution grids may capture coastal physics better. The improvement is of the same order, and in the same location, as that associated with a larger model domain.

c. Number of sigma levels

In deep water, the upper ocean is poorly resolved unless a large number of σ levels are used. In very shallow water, a small number of levels can produce acceptable vertical resolution. If the vertical resolution of the σ coordinate system is increased near the upper surface (grid stretching), some improvement can be made for deep water, but unreasonably thin upper levels can result in shallow water if grid stretching is applied uniformly over the model domain. Since the σ-coordinate system does not permit fixed resolution near the surface, it is necessary to compromise between the availability of computer resources and these depth-dependent requirements. Run 55 uses 10 σ levels, with a surface resolution of 0.17 m for the shallowest depths and 72 m for the deepest. When 20 levels are used, as in run 56, the surface σ level for the shallow and deep limits decreases in thickness to 0.06 and 26 m, respectively. The increased resolution of run 56 does not improve model accuracy; SD_A increases from 63.5% to 73.1%, with the greatest increase west of the storm track (moorings 18 and 19) and for deep water (mooring 12). There is no significant change in TD_A or RI_A (Table 6). By the above quantitative measures, it would appear that increased vertical resolution has the primary effect of increasing near-surface peak current errors.

d. Surface stress

Calculating the surface stress is a fundamental problem in applications of coastal ocean models (Broche and Forget 1992). The most popular approach for calculating the surface stress is the bulk coefficient method, in which the wind stress $\tau = C_d\rho_a U^2$, where C_d is the drag coefficient, ρ_a is the air density, and U is the wind speed at some height, usually 10 m. A constant drag coefficient is the simplest approximation of the complex momentum exchange processes between the atmosphere and the ocean, and a baseline model hindcast using $C_d = 0.002$ (run 59) will be used for comparisons of model skill as a function of surface drag formulation.

Plotting drag coefficients as a function of wind speed from a number of different studies reveals a statistically significant trend of increasing C_d with the wind speed (Huang et al. 1986). The trend is weak, however, and there is evidence that the wave state also is an important source of variability in the data. In choosing a wind-dependent bulk drag coefficient, we use a typical formulation, developed specifically from tropical storm data (Miller 1966):

$$\begin{aligned} C_d &= 0.0011, \\ &\qquad U_{10} \le 6 \text{ m s}^{-1}, \\ C_d &= [0.61 + (0.063 \times U_{10})]10^{-3}, \\ &\qquad 6 \text{ m s}^{-1} < U_{10} \le 22 \text{ m s}^{-1}, \\ C_d &= [1 + (0.07 \times U_{10})]10^{-3}, \\ &\qquad U_{10} > 22 \text{ m s}^{-1}, \end{aligned} \tag{6}$$

TABLE 5. Normalized peak surface current timing differences, TD (%).

		Experiment no.										
Mooring	T_s*	55	56	57	58	59	61	62**	72	81	85	87	88	89**
12	10.1	−20.2	−20.2	−20.2	−20.2	−23.6	−23.6	−16.7	−32.4	−22.6	−22.6	−35.2	−27.6	−20.0
13	10.3	−6.51	−6.51	−6.51	−6.52	−6.51	−9.77	−8.14	−9.53	−9.77	−9.77	−9.77	−12.1	−7.21
14	20.4	−4.23	−5.06	−5.06	−5.06	−4.23	−4.23	−1.65	−4.70	−5.06	−5.06	−8.71	−2.47	−6.23
18	14.7	−6.87	−8.02	−8.02	−8.02	−33.4	−50.6	0.00	−15.4	−13.9	−17.3	−37.2	−70.9	−375.0
19	15.6	3.23	3.23	3.23	3.23	1.08	3.23	−2.15	0.00	1.54	1.54	52.0	−60.1	8.15
TD_A	14.2	−6.93	−7.32	−7.32	−7.32	−13.3	−17.0	−5.72	−12.4	−9.96	−10.6	−7.78	−34.6	−80.1
TD_R	—	8.48	8.43	8.43	8.43	14.5	21.1	6.85	12.5	9.11	9.60	36.0	29.8	165.0

* Storm current duration in hours (see text for explanation).
** Incomplete hindcast.

where U_{10} is the wind speed at 10 m. This formulation is applied in run 61. The errors for surface current magnitudes (Table 4) increase significantly over run 59. The reliability indices (Table 6) indicate that, where wind stresses are greatest (east of the storm track), surface performance is reduced, while model skill near the bottom is improved.

Johnson and Vested (1992) use the characteristics of the wave field and water depth to compute C_d. This method worked reasonably well for an extratropical storm within the Middle Atlantic Bight (Keen and Glenn 1995). Based on the dramatic increase in error in run 62 (see Tables 4, 5, and 6), however, this formulation appears to be unsatisfactory for very large waves. The failure of these more physics-based approaches may indicate other problems with the model formulation that prevents the use of very large wind stresses near the eye.

e. Bottom stress

Bottom stress in shallow water is dependent on sediment type, bed forms, steady currents, and oscillatory wave currents; thus, it is a time-dependent, spatially varying term in the momentum equations. Because of the difficulties in constraining many of the variables that control bottom friction, it is often represented by a quadratic drag law, $\tau_b = \rho(u_{*c})^2 = \rho C_b|u_r|u_r$, where ρ is water density, u_{*c} is a friction velocity, C_b is a drag coefficient, and u_r is a reference velocity within the bottom boundary layer. Evaluating the usual logarithmic profile equation for the velocity at the reference height z_r and substituting into the equation for τ_b, the drag coefficient can be related to the bottom roughness: $C_b = [\kappa/\ln(30z_r/k_{bc})]^2$, where κ is von Kármán's constant (0.4) and k_{bc} is the apparent bottom roughness. For a discussion of the relationship between C_b and the bottom boundary layer parameters, see Keen and Glenn (1994). Whereas values of k_{bc} can be chosen based on estimated bottom and wave-current flow conditions, the present study neglects the variability of k_{bc}. Constant values of k_{bc} equals 0.001, 0.01, and 0.1 m, spanning a wide range of expected conditions, are used. For a typical reference height z_r of 1 m, C_b equals 0.0015, 0.0025, and 0.0049, respectively; however, since the reference height (middle of the lowest σ level) is a variable in the model, the drag coefficient varies spatially (but not temporally).

A good index of the effect of increasing bottom roughness is the peak surface current speed difference SD in shallow water (Table 4). For k_{bc} equal to 0.001 m (run 58), SD is 128% at mooring 14, increasing by 1% when k_{bc} is increased to 0.1 m (run 57). The value of SD at the bottom current meter (not listed in Table 4) increases by 1.3% as k_{bc} is increased from 0.001 to 0.1 m. These changes are not significant, but the trend is opposite to that expected, that is, increasing bottom friction should decrease currents throughout the water column. It is not surprising that the upper and lower

TABLE 6. Reliability indices for current magnitudes for YD 237.3 to YD 238.9.

Mooring/ depth	Experiment no.												
	55	56	57	58	59	61	62[a]	72	81	85	87	88	89[a]
12/12	2.35	2.42	2.42	2.42	2.26	2.48	2.59	2.23	2.32	2.22	2.71	2.26	2.48
12/100	4.03	3.83	3.82	3.83	3.78	3.66	5.52	4.90	4.22	4.23	4.98	4.00	7.84
13/12	2.07	2.03	2.03	2.03	1.87	2.06	2.21	1.98	2.02	2.04	2.31	2.13	2.16
13/100	2.32	2.46	2.47	2.47	2.30	2.85	3.88	2.12	2.32	2.29	2.99	2.50	2.98
13/190	3.65	3.69	3.68	3.69	3.90	3.72	6.01	2.75	2.80	2.48	3.21	2.56	3.27
14/11	1.74	1.79	1.80	1.79	1.70	1.96	1.79	1.72	1.75	1.62	1.86	1.74	1.56
14/37	2.13	2.18	2.15	2.21	2.43	2.26	2.23	2.30	2.45	2.47	2.13	2.12	1.86
15/17	2.04	2.23	2.17	2.28	1.99	2.43	2.30	2.18	1.97	2.06	2.02	2.01	2.11
18/10	1.68	1.86	1.74	1.96	1.80	1.84	2.00	1.62	1.80	1.78	2.45	2.22	2.06
18/19	5.06	4.42	4.81	4.23	4.02	4.22	4.30	2.05	2.01	2.41	2.08	2.27	2.31
19/3	2.19	2.13	2.10	2.19	1.77	2.11	1.74	1.95	1.75	1.74	1.78	2.00	1.94
19/47	3.07	3.03	3.10	2.99	3.60	4.49	4.67	2.12	2.27	2.61	2.80	2.43	2.76
RI_A[b]	2.01	2.05	2.02	2.08	1.88	2.09	2.07	1.90	1.93	1.88	2.22	2.07	2.04
RI_A[c]	2.70	2.67	2.69	2.67	2.62	2.84	3.27	2.32	2.31	2.33	2.61	2.35	2.78

[a] Incomplete hindcast.
[b] Surface moorings.
[c] All moorings.

current meters respond in a similar way to increasing bed roughness, however, because the lower current meter at mooring 14 is located 10 m above the bed. The upper current meter at mooring 15 (water depth is 20 m) stopped operating before peak currents were attained, but the magnitude of SD at the bottom meter, located 3 m above the bed, decreases from 140% to 117% as k_{bc} is increased from 0.001 to 0.1 m. This tendency is seen in RI also, which decreases from 2.28 to 2.17. The combination of bottom currents and waves that existed at moorings 14 and 15 during the storm would have increased sediment transport, thereby enhancing the apparent bottom roughness. The improvement in both indices for the bottom current meter at mooring 15 suggests that this did occur, at least in very shallow water.

Moorings 18 and 19 are located west of the storm track, where currents and waves remained smaller than at the eastern moorings throughout the storm. Mooring 18 is situated in a water depth of 22 m, and the placement of the current meters is the same as at mooring 15 (see Table 2). Surface currents at mooring 18 are overpredicted in runs 56, 57, and 58 (Table 4), although increasing the bottom roughness improves model performance by approximately 10%. The model-calculated bottom currents at mooring 18 are lower than the observed values, and increasing k_{bc} from 0.001 to 0.1 m does not significantly increase the model error. The reliability indices (Table 6) follow the pattern seen in SD, improving at the surface and deteriorating at the bed for increasing k_{bc}. The error indices at mooring 19 (water depth is 51 m) follow the same trend as at mooring 18. The error tendencies at the shallow water moorings suggest that a large apparent bottom roughness is appropriate during the storm, although it was not uniformly distributed.

f. Turbulent mixing

The model currents at the surface current meters are generally too high in all water depths, and the purpose of the experiments discussed in this section is to increase vertical momentum exchange, especially at deep water moorings where stratification is strong. Moorings 12 through 15 are on the right side of the storm track where the highest wind speeds occur, and the model-predicted peak surface currents are higher than the observed currents at all of these moorings. The lower current meters at moorings 12 and 13, at a depth of 100 m, are below the storm-influenced surface layer. These moorings cannot, therefore, be used to examine near-surface vertical mixing. Mooring 15 also cannot be used because of the incomplete record from the surface current meter. The values of SD at mooring 14 (run 57) are 129% at the surface (Table 4) and 55.7% at the bottom (not listed). Storm winds were consistently weaker at moorings 18 and 19, and turbulent mixing was presumably less intense than at mooring 14. The complete records for water depths of 22 and 51 m allow vertical mixing processes to be examined comprehensively for a variety of conditions. The peak hindcast surface currents at mooring 19 are 101% high, whereas the bottom currents are 65.7% too low (not listed). The model-predicted high surface and low bottom currents relative to the observations at moorings 14 and 19 can be partly attributed to insufficient vertical turbulent mixing of momentum.

1) TURBULENCE DISSIPATION

The MY2.5 turbulence model incorporates an equation for turbulent kinetic energy that includes both shear and buoyancy production terms, as well as a dissipation term given by

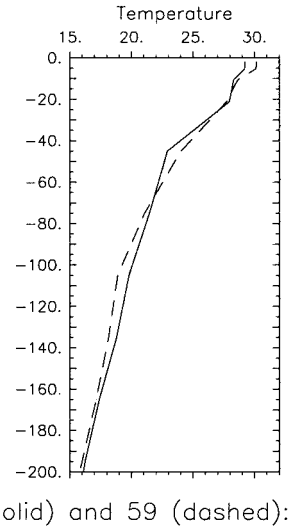

FIG. 7. Poststorm temperature profiles of the upper 200 m for run 57 (solid line) and run 59 (dashed line) at mooring 12.

$$\varepsilon = q^3/(B_1 l), \tag{7}$$

where q^2 is the turbulent kinetic energy, l is a mixing length, and B_1 is an empirical constant. The dissipation term is derived by assuming that the flow is two-dimensional, production equals dissipation, and buoyancy effects are negligible (Mellor and Yamada 1982). The value of the constant B_1 has been determined to range from 12.17 to 25.67 for laboratory flows where production equals dissipation in the absence of stratification (e.g., the overlap region near walls and in homogeneous shear flow), and an intermediate value of 16.6 is recommended by Mellor and Yamada (1982). Vertical turbulent mixing can be enhanced in the MY2.5 model by decreasing dissipation in (7) through the constant B_1. All of the experiments discussed in this paper use a stratified water column, and it is of interest that a critical Richardson number, where vertical turbulent mixing of momentum and heat is zero, increases with the value of B_1. This has the effect of increasing turbulent mixing where a vertical density gradient exists.

To examine the effect of increasing B_1, an experiment using a value of 16.6 (run 57) is compared to an experiment with $B_1 = 40$ (run 59). Other constants in the MY2.5 turbulence closure model use the values suggested by Mellor and Yamada (1982). The initial depth of the thermocline at mooring 13 is approximately 20 m (Fig. 6) with a uniform mixed layer temperature of about 30°C. The surface temperature (Fig. 7) is 1°C higher in run 59 than in run 57, suggesting that turbulent mixing above 10 m is reduced with decreased turbulence dissipation. This result can be attributed to the homogeneous initial temperature profile near the surface. A shallow thermocline is present at a depth of 10 m in both runs. The temperature profile below this depth is much smoother when dissipation is decreased, and the lower thermocline at 50 m predicted in run 57 is absent in run 59. The change in the temperature profile of run 59 is the result of enhanced mixing at the initial thermocline depths of 20 and 50 m. This enhanced mixing at middepths has produced a new lower thermocline extending to 100 m in run 59. No measured temperature profiles are available after the hurricane, and it is not possible, using the mooring data alone, to determine which of the two profiles in Fig. 7 is correct.

The larger value of B_1 improves hindcast performance at all moorings, as measured by surface current speed differences (Table 4). At the deep water moorings, SD decreases from near 50% for the standard turbulence parameters to almost nil. Speed differences also decrease significantly to the west of the storm track (moorings 18 and 19). Peak current timing differences TD (Table 5) increase slightly everywhere except at mooring 18.

The combined time–space performance of the model, as indicated by RI_A (Table 6), improves overall with a decrease in turbulence dissipation. Model-predicted surface currents are better everywhere except at mooring 18. Moorings 12 and 13 show improvement above 100 m, indicating that increased turbulent mixing is effective at improving the current profile in the upper water column where a large density gradient is found. Moorings 14 and 19 are in water depths of approximately 50 m, where the initial thermocline is located near the bed. Increased mixing very near the bottom causes the hindcast current profile in run 59 to be more uniform than suggested by the measured currents. As a result, the reliability indices at moorings 14 and 19 are smaller at the surface and larger at the bottom, when turbulent mixing is increased. Moorings 15 and 18 are located in water depths of 20 m, and RI values decrease for the bottom currents at both locations. The RI value increases near the surface at mooring 18, but the incomplete record for the surface current meter at mooring 15 does not permit a comparison at this mooring. Nevertheless, the implication is that, for water depths shallower than the thermocline, near-surface mixing may be insufficient, while mixing near the bottom improves near-bed currents in the model.

Despite the assumptions employed in the derivation of (7), the MY2.5 model gives reasonable results in the wave-affected layer for unstratified conditions (Craig and Banner 1994). Under conditions of strong wave forcing and stratification, however, the boundary layer approximation is less applicable, and adjusting the constant B_1 cannot make up for additional turbulent energy dissipation due to wave energy input. Increasing B_1 is intended to augment near-surface mixing in deep water where excessive current shear is most apparent in the model.

2) WAVE-ENHANCED TURBULENCE

The MY2.5 model does not incorporate wave breaking as a source of turbulent kinetic energy q^2 near the

upper surface (Craig and Banner 1994). Typically, a turbulence flux is introduced in the surface level only and mixes downward by shear-induced turbulence. For strongly forced waves, however, the turbulent energy flux into the water through wave breaking can be an order of magnitude greater than conventional estimates based on shear-generated turbulence (Terray et al. 1996). A wave-dependent scaling of the dissipation rate proposed for such strong forcing has also been confirmed for fully developed waves (Drennan et al. 1996). Despite the specification of turbulence constants determined from dominantly shear-produced turbulence regimes, dissipation rates predicted by the MY2.5 model are in agreement with measured profiles within the wave-stirred sublayer at the surface (Craig and Banner 1994). Given that the MY2.5 model gives reasonable results for a range of turbulence situations, it is convenient to address the problem of near-surface mixing through a physics-based approach.

The surface flux of turbulent kinetic energy from wave breaking can be estimated as

$$E_w \approx 4.3 \times 10^{-5} \rho U_{10}^3 (c_b/c_p)^5, \quad (8)$$

where c_b is the phase speed of breaking waves, and c_p is the phase speed at the spectral peak (Melville 1994). The uncorrected wind speed at 20 m is used in this study. The value of c_b/c_p is a function of wave age (c_p/u_{*w}, where u_{*w} is the friction velocity from wind), and it can range from 0.4 to 0.63 for spilling breakers. The value of c_b/c_p can also be computed using the wind input and wave spectrum (Terray et al. 1996), but this method is not used in the present study because wave spectra are not available. Instead, we use $c_b/c_p = 0.5$ for all grid points. The dissipation rate of this wave-breaking energy within a wave-stirred layer of depth z_w can be described by a three-layer structure (Terray et al. 1996): 1) dissipation is high and roughly constant in a breaking zone, 2) a transition layer lies below this wherein dissipation scales with z^{-2}, and 3) a deep layer where wall scaling applies. Layer 1 is on the order of H_s and is assumed equal to 0.5 H_s here. Layer 2 may be as deep as $25H_s$ for strongly forced waves (Terray et al. 1996), and a depth of $20H_s$ is used in this study.

The turbulent energy flux into the wave-stirred sublayer is given by $dq^2/dt = E_w/\rho z_w$. This turbulent energy is distributed among the model σ levels contained within wave-influenced layers 1 and 2 in the same way as dissipation. It is added to the shear-generated turbulence from the MY2.5 model. Within layer 3, q^2 is generated by shear using only the standard MY2.5 model. This approach produces large near-surface turbulence that decreases rapidly to shear-induced turbulence values with depth, which is in agreement with observations (Terray et al. 1996). This technique also introduces spatial variability through the use of available hindcast significant wave heights.

A critical scale in the MY2.5 model is the master turbulent length scale L (Mellor and Yamada 1982). For wall scaling of turbulence, L is assumed to go to zero, but this is clearly inappropriate in the presence of breaking waves. Craig and Banner (1994) have demonstrated the importance of nonzero roughness at the sea surface using the MY2.5 model. The present study does not incorporate their modified closure model. Instead of computing L as a function of water depth, as well as surface and bottom roughness heights, a simple calculation is used within the wave-influenced layer only. Within the breaking zone, $L = H_s$. Below this depth, within the transition layer, the master turbulent length scale is assumed to scale with the wave orbital diameter, $L = H_s e^{(-2\pi z/\lambda)}$, where z is the depth below the breaking zone and λ is the deep water wavelength.

The derived turbulent energy variable q^2L is subsequently calculated for all σ levels within the wave-influenced layer. Below this layer, L is computed by the MY2.5 model. The resulting discontinuity at $20H_s$ is not significant in the present study because of the relatively small mixing lengths below the wave-influenced layer.

Figure 8 shows current magnitudes from run 81 (decreased turbulence dissipation), run 87 (surface mixing from wave breaking), and the observations at the moorings. The peak currents for run 87 (long–short dash line) are shifted ahead slightly at several moorings relative to run 81. As a result, both TD (Table 5) and RI (Table 6) increase. The inclusion of wave turbulence in run 87 decreases peak surface currents significantly compared to runs with the standard turbulence closure (e.g., run 57), and the surface current speed differences (Table 4) have smaller magnitudes than run 81, except at mooring 13 where the difference is less than 3%. Figure 9 shows profiles of Q^2L and current speed at moorings 12 and 15 at YD 237.894. Since q^2L scales with the significant wave height (H_s equals 9.8 m at mooring 12, and 9 m at mooring 15), instead of going to zero at the surface, turbulence values are several orders of magnitude greater in run 87 (dash line). The current profiles for these two runs are significantly different as well. For both water depths, near-surface shear is excessive for run 81 because the larger value of B_1 primarily increases mixing at the thermocline. This is especially noticeable at mooring 15. The lack of fit between run 81 and the observations (Fig. 8) further suggests that this shear is not realistic. Unfortunately, the available measurements do not allow a more extensive evaluation of the near-surface current profile.

g. Initial temperature distribution

All of the experiments discussed so far have used profiles of salinity and temperature measured at mooring 13 on 24 August (Fig. 6) to construct horizontally uniform initial salinity and temperature fields. There were several locations where the observed conditions differed markedly from this profile, especially in shallow water. A depth-dependent initial condition for temperature has been constructed to incorporate more of the available

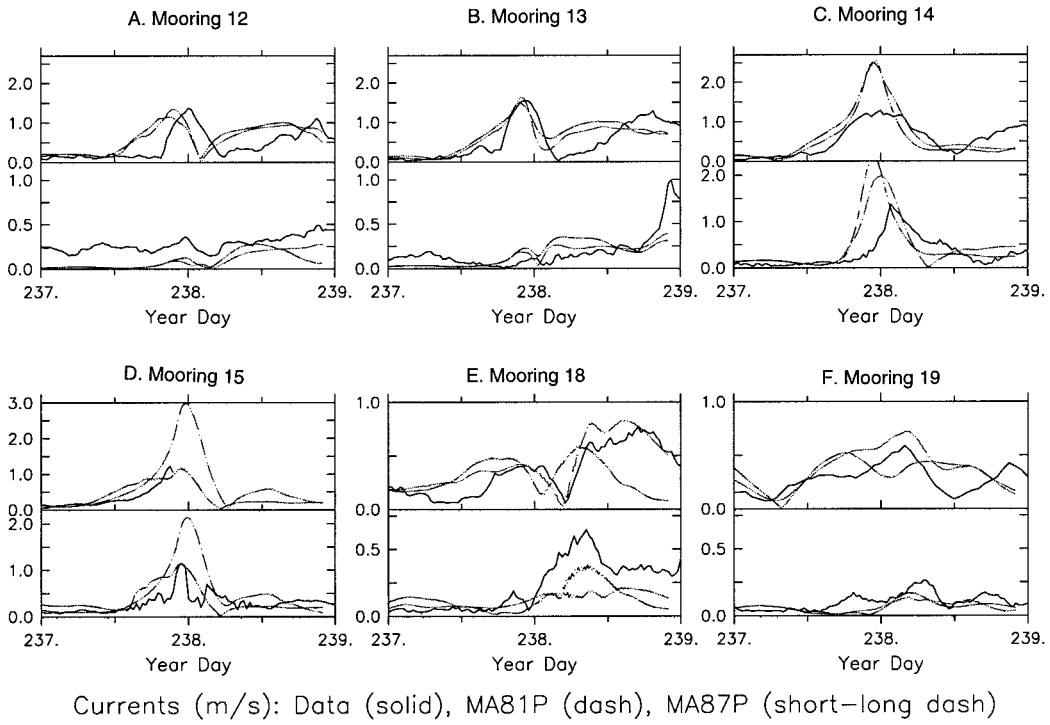

FIG. 8. Time series of current speed (m s^{-1}) for observations (solid line), run 81 (dashed line), and run 87 (short–long dashed line) at LATEX moorings.

measurements. Hydrographic data were collected on 15–20 August along an across-shelf line extending from 10- to 50-m water depths at approximately 90.5°W. These observations were combined with CTD profiles measured at moorings 12 and 13. The linearly interpolated cross section was then applied to the entire model domain, producing a water-depth-dependent initial condition for temperature (Fig. 10).

Temperature measurements at the moorings at approximately 1000 GMT 24 August are indicated by the squares in Fig. 10, and the interpolated temperatures are shown by the dashed line. Note the improved fit between the mooring data and the new profiles, especially in shallow water. Surface stratification is reduced at mooring 12 but the thermocline is unchanged. For shallower water, however, the difference in temperature profiles is significant. For moorings in about 50-m water depths (moorings 14 and 19), the temperature gradient is larger and indicates a thermocline at about 20 m below the surface. At locations in approximately 20-m water depths (moorings 15 and 18), the thermocline is present at 10 m and the water column is strongly stratified.

The influence of a depth-dependent initial temperature distribution on a model with decreased turbulence

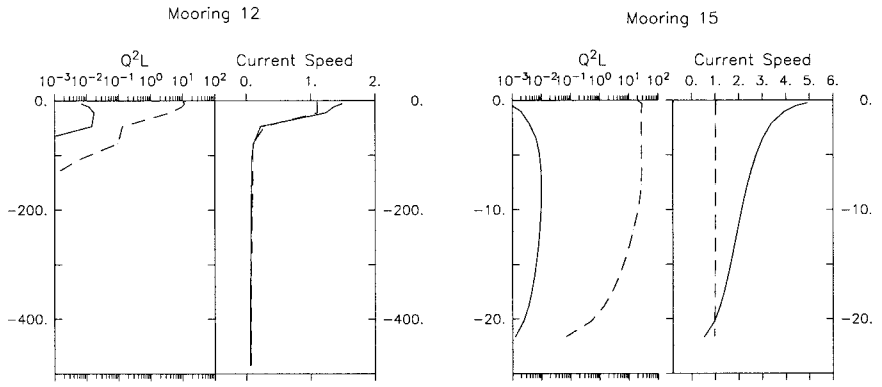

FIG. 9. Profiles of model calculated q^2L (m^2 s^{-1}) and current speed (m s^{-1}) at YD 237.894. (a) Mooring 12. (b) Mooring 15. See Fig. 2 for locations. Key: Run 81 (solid line); run 87 (dashed line).

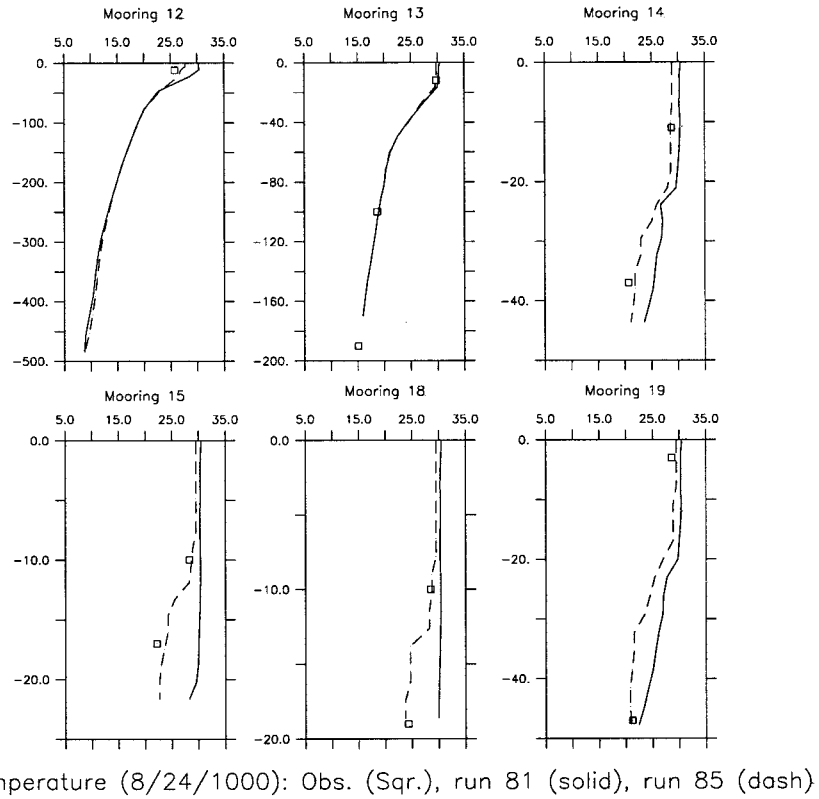

FIG. 10. Profiles of initial temperature at all moorings. The solid line is the profile in Fig. 6 (measured at mooring 12), the dashed line is the interpolated cross section discussed in the text, and the open squares are the measured values at approximately 1000 GMT 24 August.

dissipation can be examined by comparing runs 81 (horizontally uniform) and 85 (depth dependent). The surface temperature gradient at mooring 12 is smaller in run 85, and greater vertical momentum exchange occurs above the thermocline, thus reducing surface currents relative to run 81. The largest improvement in the temperature profiles, relative to the observations, is at moorings 15 and 18, but SD has increased by 3.64% at mooring 18. The reliability index for bottom currents (Table 6) is 0.4 larger at mooring 18 for the depth-dependent temperature profiles and 0.02 smaller at the surface. A similar pattern is seen at all of the shallow water moorings. The principal difference between runs 81 and 85 is a small decrease in RI surface currents and an equally small increase for bottom currents. This lack of sensitivity for the shallow water currents is caused by the increased mixing at the thermocline at the shallow moorings, making the model behave very much the same for all stratification conditions.

The influence of the depth-dependent initial temperature field on hindcasts that incorporate wave-breaking turbulence can be evaluated by comparing run 87 (horizontally uniform) and run 88 (depth dependent). Vertical mixing in the wave-influenced layer at mooring 12 is greater in run 88 because of the decreased surface temperature gradient. Surface currents are, therefore, underpredicted by 18.5% (Table 4). There is no significant change in SD at mooring 13 because the temperature profile is unaltered. The time differences (Table 5) at moorings 12 and 13 are the same for run 88 as for runs with decreased turbulence dissipation, suggesting that increased vertical mixing at any depth within the mixed layer slows the upper ocean response to the storm winds. The thermocline is better defined in shallow water for the three-dimensional initial temperature condition than for the simple stratification of run 87. As a result, peak surface currents increase while SD becomes more positive. The values of TD are more negative at all shallow water moorings. The difference has increased to -70.9% and -60.1% (early peaks) at moorings 18 and 19, respectively. Despite the early peak currents on the west side of the storm track, the reliability indices (Table 6) are smaller for run 88 everywhere except for bottom currents at mooring 18 and the surface currents at mooring 19. Here, RI_A has decreased to only 2.35, very close to the minimum value of 2.31 calculated for run 81. The systematic decrease in RI for run 88 compared to run 87 indicates that, with the inclusion of wave-breaking turbulence, the MY2.5 mixing algorithm increases the POM model's skill significantly as the initial stratification is improved.

6. Discussion

No systematic improvement in model skill resulted from a doubling of the number of σ levels for the standard MY2.5 turbulence model. However, increasing the horizontal resolution from approximately 11 to approximately 5.5 km improved model skill, as measured by peak surface current speed and timing differences, as well as reliability indices averaged over all current meters. This is especially true in areas where the model forcing is not dominated by wind stresses. These areas (e.g., west of the storm track) are characterized by more complex flow patterns that reflect the interplay of surface stresses and pressure gradients. Thus, increased horizontal resolution should be used in preference to vertical resolution if computational resources are a limiting factor. A moderate improvement in model skill is associated with the larger model domain (run 72), but this gain is not as great as that produced by a smaller cell size (run 81).

The wind- and wave-dependent surface drag coefficients used in runs 61 and 62 have the principal effect of increasing wind stresses near the radius of maximum winds. The fact that the specific methods used here were developed for either more moderate conditions or as tropical storm averages may explain why model performance deteriorated when they were implemented.

There is no significant improvement in average skill as k_{bc} is increased from 0.001 to 0.1 m. The larger apparent bottom roughness represented by $k_{bc} = 0.1$ m implicitly represents wave–current effects, although these are not explicitly included in the bottom drag formulation. Thus, combined wave–current bottom shear stresses at moorings 14 and 15, which are located east of the storm track where wind stresses (Fig. 3) and significant wave heights (Fig. 4) remain consistently large throughout the storm, would have generated larger bedforms and wave–current interactions, thereby increasing k_{bc}. The larger value is, therefore, appropriate for this area, as indicated by the low values of RI at moorings 14 and 15 for $k_{bc} = 0.1$ m and the large error for $k_{bc} = 0.001$ m. Storm waves remained moderate west of the storm track and, as a result, the larger value of k_{bc} increased the error at moorings 18 and 19. The simple bottom drag coefficient used in the model does not account for time-dependent changes in the wave field and bottom roughness.

Decreasing turbulence dissipation (and increasing thermocline mixing) in run 59 did not dramatically decrease RI_A (compare to run 57, Table 6), but it did substantially decrease surface current speed differences at all moorings. When a smaller cell size was used in addition to decreased dissipation (run 81), the smallest RI_A among all runs resulted. Incorporating wave-breaking turbulence while using the same temperature and salinity initial condition (run 87) did not significantly improve model skill. For the simple initial condition used for most of these runs, a decrease in cell size accompanied by a decrease in turbulence dissipation appears to be the best numerical approach. This outcome is partly explained by comparing current profiles at mooring 19 (Fig. 11). The current profile from run 81 (solid line) reveals excessive near-surface shear indicative of insufficient mixing for the existing wind conditions. The along-shelf currents at 3-m depth are very close to the measurements (squares), while across-shelf currents are slightly high. The same profiles for run 87 (dashed line) are representative of a wind mixed layer 17 m deep. Although the alongshore component is correct, across-shore currents are half the measured value. The implication is that wave-breaking turbulence and/or the near-surface mixing length are being overestimated in run 87. Since the model (run 87) uses a simple function of the significant wave height for turbulent mixing variables, it is possible that this characteristic of the wave field may have been overpredicted at this location. It is also probable that c_b/c_p, the ratio of phase speeds of breaking waves and peak waves, varies significantly between the moorings from the value of 0.5 used uniformly in the model.

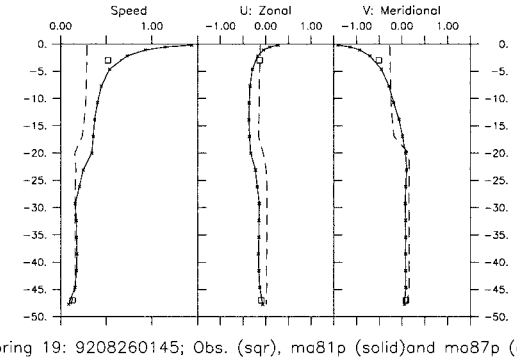

FIG. 11. Profiles of currents at mooring 19 at YD 238.06 (08/26/0145 GMT) Left: magnitude, Center: east–west component, and Right: north–south component. Key: Measurement at current meters (squares), run 81 (solid line), and run 87 (dashed line).

The improvement in the initial temperature field with use of a water-depth-dependent distribution (Fig. 10) is noticeable, but when this initial condition was used with the standard MY2.5 mixing (run 89), one of the largest values of RI_A was produced in this study. When turbulence dissipation was decreased (run 85), model skill improved significantly, but no more than for the simple initial temperature condition (run 81). This is caused by factors discussed in section 5g. With the incorporation of wave breaking (run 88), model skill becomes comparable with the best case. This result suggests that the use of the best possible initial condition improves model skill the most when more realistic model physics are incorporated.

The two model skill indices used in this study describe different aspects of a model's performance. Peak analysis focuses on a maximum signal, whereas a comparison of time series describes more general perfor-

mance during the hindcast interval. At times, a significant improvement in skill is seen for peak surface currents, while RI remains very similar (e.g., increased thermocline mixing in run 59). For most cases, however, the two types of skill parameters shift in the same direction but with different changes in relative magnitude.

7. Conclusions

This study uses quantitative skill indices to analyze improvements in performance of a three-dimensional, turbulent energy, primitive equation model for coastal seas (Princeton Ocean Model). The focus is on currents during the passage of Hurricane Andrew across the Louisiana continental shelf. Skill parameters describing the model's ability to match observed maximum surface currents, and time series at several depths and locations, have been described and used to evaluate the following model parameters: 1) model domain size; 2) horizontal resolution, including the bathymetry and coastline; 3) vertical resolution (i.e., number of model levels); 4) the surface drag formulation; 5) the bottom drag coefficient; 6) turbulent mixing parameters and sources of turbulence; and 7) initial temperature field. This procedure allows answers to be given to the questions posed in section 1.

1) Model-predicted currents are in good agreement with observations at most of the moorings. Performance is better where currents are primarily wind driven (i.e., to the east of the storm track). Complex interactions of baroclinic and barotropic flows degrade the model's skill to the west of the storm track. Model performance is in general better near the surface, especially in water depths of 200 m or more.
2) The best overall performance is produced by ''tuning'' the closure scheme to decrease turbulence dissipation and improve mixing at the thermocline. Results are almost as good when wave-breaking turbulence is included in the model, and an improved initial temperature distribution is used. The wave-breaking model is more responsive to changes in the initial temperature distribution.
3) One of the most important results of this study has been the incorporation of wave breaking as a source of near-surface turbulence in the MY2.5 turbulence model. The inclusion of this important turbulence source systematically improves the model's skill when strongly forced waves are present.

Despite the improvements in model performance that have been discussed in this study, there are at least two issues that remain to be resolved: 1) there remains a problem with vertical mixing when the wave field is not adequately described by the significant wave height and peak frequency and 2) there is an obvious need to include combined wave–current bottom stresses and turbulence generation at the bed in very shallow water. Addressing these two problems would more fully incorporate the influence of waves on shallow water flows.

Acknowledgments. The first author was funded under the Naval Research Laboratory Very High Resolution 4-D Coastal Ocean Currents project, Program Element 62435N of the Office of Naval Research. The second author was funded by the Middle Atlantic Bight National Undersea Research Center (MAB96-10, NYB94-7) and the Office of Naval Research (N00014-95-1-0457). LATEX mooring data were supplied by the Minerals Management Service (MMS), although the contents of this paper do not necessarily reflect the policies of the MMS. This work was supported in part by a grant of High Performance Computer (HPC) time from the Department of Defense HPC Shared Resource Centers at the Naval Oceanographic Office and the U.S. Army Corps of Engineers Waterways Experiment Station.

REFERENCES

Bedford, K. W., and J. Lee, 1994: Near-bottom sediment response to combined wave-current conditions, Mobile Bay, Gulf of Mexico. *J. Geophys. Res.,* **99,** 16 161–16 177.

Broche, P., and P. Forget, 1992: Has the influence of surface waves on wind stress to be accounted for in modeling the coastal circulation. *Estuarine Coastal Shelf Sci.,* **35,** 347–351.

Cardone, V. J., A. T. Cox, J. A. Greenwood, D. J. Evans, H. Feldman, S. M. Glenn, and T. R. Keen, 1994: Hindcast study of wind, wave and current fields in Hurricane Andrew, Gulf of Mexico. Final Rep. to Minerals Management Service, 150 pp. [Available from Procurement Operations Branch, Mail Stop 2510, 381 Elden St., Herndon, VA 22070-4817.]

Craig, P. D., and M. L. Banner, 1994: Modeling wave-enhanced turbulence in the ocean surface layer. *J. Phys. Oceanogr.,* **24,** 2546–2559.

Drennan, W. M., M. A. Donelan, E. A. Terray, and K. B. Katsaros, 1996: Oceanic turbulence dissipation measurements in SWADE. *J. Phys. Oceanogr.,* **26,** 808–815.

Forristall, G. Z., R. C. Hamilton, and V. J. Cardone, 1977: Continental shelf currents in Tropical Storm Delia: Observations and theory. *J. Phys. Oceanogr.,* **7,** 532–546.

Huang, N. E., L. F. Bliven, S. R. Long, and P. S. DeLeonibus, 1986: A study of the relationship among wind speed, sea state, and the drag coefficient for a developing wave field. *J. Geophys. Res.,* **91,** 7733–7742.

Johnson, H. K., and H. J. Vested, 1992: Effects of water waves on wind shear stress for current modeling. *J. Atmos. Oceanic Technol.,* **9,** 850–861.

Keen, T. R., and R. L. Slingerland, 1993: A numerical study of sediment transport and event bed genesis during Tropical Storm Delia. *J. Geophys. Res.,* **98,** 4775–4791.

——, and S. M. Glenn, 1994: A coupled hydrodynamic-bottom boundary layer model of Ekman flow on stratified continental shelves. *J. Phys. Oceanogr.,* **24,** 1732–1749.

——, and ——, 1995: A coupled hydrodynamic-bottom boundary layer model of storm and tidal flow in the Middle Atlantic Bight of North America. *J. Phys. Oceanogr.,* **25,** 391–406.

——, and ——, 1996: A quantitative skill assessment of numerical hydrodynamic models of coastal currents. *Proc. 4th Intl. Conf. Estuarine and Coastal Modeling. IV,* San Diego, CA, A.S.C.E., 26–40.

Leggett, R., and L. Williams, 1981: A reliability index for models. *Ecol. Modell.,* **13,** 303–312.

Martin, J., 1988: Application of a two-dimensional water quality model. *J. Environ. Eng.*, **114,** 317–336.

Mellor, G. L., 1993: Users guide for a three-dimensional, primitive equation, numerical ocean model. Rep. to the Institute of Naval Oceanography, 35 pp. [Available from Atmospheric and Oceanic Sciences Program, Princeton University, Princeton, NJ 08540.]

——, and T. Yamada, 1982: Development of a turbulence-closure model for geophysical fluid problems. *Rev. Geophys. Space Phys.*, **20,** 851–875.

Melville, W. K., 1994: Energy dissipation by breaking waves. *J. Phys. Oceanogr.*, **24,** 2041–2049.

Miller, B. I., 1966: Energy exchanges between the atmosphere and the oceans. *Hurricane Symposium.* Vol. 1, American Society of Oceanography, 134–157.

Spaulding, M. L., and T. Isaji, 1987: Three-dimensional continental shelf hydrodynamics model including wave current interaction. *Three-Dimensional Models of Marine and Estuarine Dynamics*, J. C. J. Nihoul and B. M. Jamart, Elsevier, 405–426.

Terray, E. A., M. A. Donelan, Y. C. Adrawal, W. M. Drennan, K. K. Kahma, A. J. Williams III, P. A Hwang, and S. A. Kitaigorodskii, 1996: Estimates of kinetic energy dissipation under breaking waves. *J. Phys. Oceanogr.*, **26,** 792–807.